Computational techniques for modelling noise in AC susceptibility measurements on nonlinear materials

Darren W. Lim*

13 May 2024

Abstract

AC magnetic susceptometry is a very well-established technique in experimental condensed matter research. Performed properly, this methodology is robust and noise-resistant, with wide applications on many materials. However in practice there will always be some degree of noise, which limits the measurement's sensitivity. These noise sources are difficult to analyse, as they depend on many possible factors.

A computational model simulating the experimental setup from first principles could – if the fidelity is sufficiently high – accurately predict the effects of various noise sources. This would be useful for placing upper bounds on the achievable precision for a given setup, and can also help to inform experimenters in designing setups to minimize or mitigate noise.

In this work, I discuss the mathematical and computational principles underlying how an AC susceptometer can be realistically modelled, and how the expected measurements from the setup can be numerically predicted. Particular focus is placed on nonlinear materials, which violate typical simplifying assumptions, and how a model can be constructed without such assumptions.

1 Introduction

The (differential) AC magnetic susceptibility of a material is an important measure of its magnetic properties, and is defined as the tensor:

$$\chi_{ij}(\omega) \ = \ \frac{\partial M_i}{\partial H_j}$$

where $\mathbf{H}$ is an applied AC field of angular frequency ω with some DC background, and $\mathbf{M}$ is the material's magnetization (which need not be a single-valued function of $\mathbf{H}$). In general $\chi_{ij}(\omega)$ is diagonalizable, and can be treated as a scalar along the principal axes.[1,2]

The accurate measurement of $\chi(\omega)$ has many applications – e.g. in detecting phase transitions,[3] identifying material phases,[4] obtaining band structures via de Haas-van Alphen spectroscopy,[5,6] etc.. Furthermore, it can be measured using a relatively simple setup, with the technique being well-established.[7] As such, AC susceptometry serves as a standard tool in experimental condensed matter research.[8]

However, no tool is perfect, and the precision of an AC susceptometer will generally be limited by certain effects. These include, non-exhaustively:

1. Mechanical vibration;[6,7]

2. External electromagnetic radiation;
   in particular from mains noise;

3. Eddy currents;[9]

4. Thermal dissipation;

5. Impedance mismatch;

6. Johnson-Nyquist noise.[10]

These effects cause both systematic errors and random noise. Critically, while effects #5 and #6 are simple enough to analyse on paper, effects #1 through #4 cannot be easily predicted by hand from experimental parameters.

Instead, predictions must be made numerically, by constructing a high-fidelity computational model of the AC susceptometer from first principles. This would be useful for studying the impact of these noise sources, placing upper bounds on achievable sensitivities for a given setup; it may also help experimenters develop design strategies to minimize or mitigate noise.

In this work, I discuss the principles underlying how an AC susceptometer can be realistically modelled, with a computational approach in mind; this work is structured as a concept review that the reader may consult for constructing their own model. Focus is placed on nonlinear materials, as they are important in the condensed matter context. The effects of #1, #2, and #5 on the susceptometer's key observable – namely, phase-sensitive AC voltage – are estimated at first order.

---
*Supervisors: Suchitra Sebastian, Nicholas J.M. Popiel, Jiasheng Chen

2 Typical construction of an AC susceptometer

An AC susceptometer consists of at least three coils:

- A *drive coil**, which is responsible for subjecting the sample to a controlled H field. The drive coil is sometimes split into two separate coils (with independent controllers), with one coil producing the DC component and another† producing the AC component of the H field.

- A *sample coil*‡, which is wound around the sample, and senses the variations of magnetic flux;

- A *reference coil*§. The sample and reference coils are collectively known as the *secondary coils*.[11]

The reference coil is connected in opposition to the sample coil, so as to cancel the voltages induced by the vacuum flux of the H field itself, as well as that induced by external sources. Both secondary coils are immersed within the drive coil, with the reference coil typically designed to have equal flux area (i.e. loop area multiplied by number of turns) with the sample coil; the coils are said to be *balanced* if so.

There are two common configurations for the secondary coils: *coaxial*, where the sample and reference coils are placed end-to-end, and *concentric*, where the reference coil is wound over the sample coil. See fig. 1 and fig. 2. The coaxial configuration is popular amongst classroom demonstrations owing to its simplicity; however, independent vibrations of the coils can generate significant noise. The concentric configuration is therefore preferred for laboratory use, with its superior signal-to-noise ratio, despite the signal being suppressed by a factor of the turn number difference between the two coils.[6]

The total series voltage of the secondary coils are typically fed into a lock-in amplifier, which is phase locked to the AC component of the H field. (See fig. 3.) Hence the measured signal contains only the AC voltage components within a narrow range of the H field's angular frequency ω, and its amplitude is directly proportional to the AC magnetic susceptibility $\chi(\omega)$. While the proportionality constant can hypothetically be calculated from the setup, in practice it is experimentally calibrated against a known standard, e.g. a SQUID.[9]

The principle of operation of the AC susceptometer is detailed in appendix A.

---

*Also known as the *primary coil* in literature.
†This one is known as the *modulation coil*, if it is separate.
‡Also known as the *pickup coil* in literature.
§Also known as the *compensator coil* in literature.
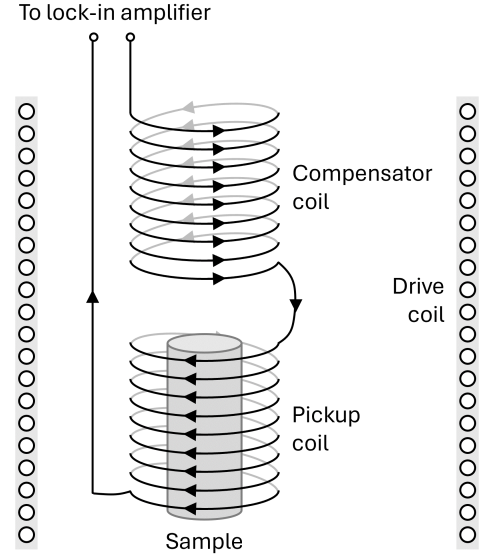

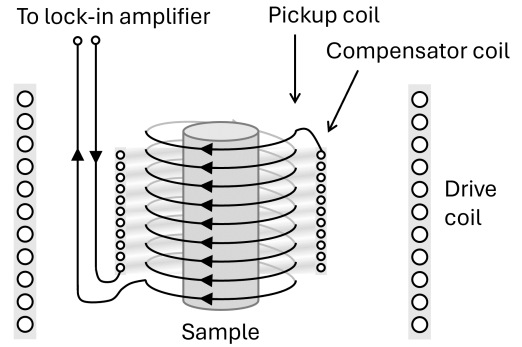Fig. 1: Schematic of a coaxial configuration AC susceptometer.

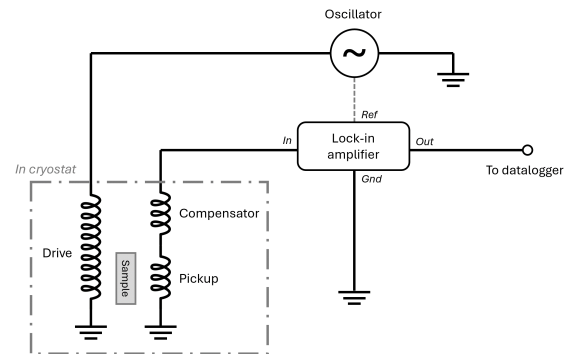Fig. 2: Schematic of a concentric configuration AC susceptometer.

Fig. 3: Simplified circuit diagram for a typical AC susceptometer.

3 Computation of electromagnetic fields

To simulate the behaviour of a realistic AC susceptometer, we require a model of the electromagnetic fields. In principle, Maxwell's Equations[12] can be fully solved for all regions of space, provided appropriate boundary conditions and the material responses $\mathbf{P}(\mathbf{E})$, $\mathbf{M}(\mathbf{H})$ at all points of space:

$$\nabla \cdot \mathbf{D} \;=\; \rho_f \quad ; \qquad \nabla \times \mathbf{E} \;=\; -\frac{\partial \mathbf{B}}{\partial t} \quad ;$$
$$\nabla \cdot \mathbf{B} \;=\; 0 \quad ; \qquad \nabla \times \mathbf{H} \;=\; \mathbf{J}_f + \frac{\partial \mathbf{D}}{\partial t} \quad .$$

These equations may hypothetically be coupled to all phenomena of interest, e.g. simultaneously accounting for time-varying positions of the materials to model vibrations, and adding external distant sources to model electromagnetic noise.

However, a full solution would be infeasible, as experimental externalities introduce indeterminate boundary conditions. This approach would require "solving for the whole universe" to produce any predictions.

Instead, a *perturbative* approach must be taken, where we first solve for the magnetic fields under ideal conditions, and then study each phenomenon of interest independently by adding their effect as a perturbation. This approach is particularly applicable for predicting random noise, as different noise sources can be assumed to be uncorrelated.

3.1 The magnetostatic limit

Since electrostatics are not within the scope of interest, we turn our focus towards the $\mathbf{B}$ and $\mathbf{H}$ fields. The electric fields may effectively be neglected, except in the calculation of measured voltages at the end.

If the system's lengthscale is much shorter than the speed-of-light propagation within the shortest timescale of interest (which can be estimated as c/ω), the Maxwell addition to Ampère's Law may be safely neglected – formally, this is achieved by taking the limit $c \to \infty$.[13] This leaves the magnetostatic equations:

$$\nabla \cdot \mathbf{B} \;=\; 0 \quad ; \quad \nabla \times \mathbf{H} \;\approx\; \mathbf{J} \quad . \tag{1}$$

In particular, the Biot-Savart Law provides a general solution to Ampère's Law:

$$\mathbf{H}(\mathbf{r}, t) \;\approx\; \int d^3\mathbf{r}' \, \frac{\mathbf{J}(\mathbf{r}', t) \times (\mathbf{r} - \mathbf{r}')}{4\pi |\mathbf{r} - \mathbf{r}'|^3} \quad . \tag{2}$$

Consider a closed curve $\partial \Sigma$, e.g. a coil, forming a boundary of an open surface Σ. The voltage differential measured across $\partial \Sigma$ is given by:

$$V_{\partial \Sigma}(t) \;=\; \oint_{\partial \Sigma} \mathbf{E} \cdot d\mathbf{l} \;=\; -\frac{d}{dt} \iint_{\Sigma} \mathbf{B} \cdot d\mathbf{S} \quad . \tag{3}$$

Hence, the scope of the problem has been greatly reduced: from the supplied currents $\mathbf{J}$ in the drive coil as a function of space and time, the $\mathbf{H}$ field can be calculated everywhere using eq. (2); then the $\mathbf{B}$ field may be obtained from the material's response with appropriate interface conditions. Finally eq. (3) can be used to predict the measured voltage through the secondary coils.

3.2 Modelling coils realistically

To the simplest approximation, a coil with N turns of radius R over length l (such that $NR \gg l \gg R$) can be modelled as an ideal solenoid; in which case the H field produced by current I is spatially uniform and given by $H = NI/l$, while the magnetic flux Φ for a volume-averaged $\langle B \rangle$ field is $\Phi = \pi R^2 N \langle B \rangle$.[12]

However a realistic model of noise requires that the H field produced by the drive coil, and the flux passing through the secondary coils, are modelled accurately. In particular the following considerations are important:

- Finite coil length, giving edge effects near the ends;

- Finite turn density, giving non-uniform field near the radial boundary;

- Non-zero wire thickness, over which current density is spatially distributed;

- Helicity $L/2\pi NR$, which gives a "twist" component to the field;

- Skin effect, which concentrates current density towards the outer surfaces of wires.

It suffices, in the computational model, to treat a coil as a single, continuous, right-handed helix centred on the origin and aligned along the z-axis; more general cases can then be assembled by rotations, translations, and additions of multiple helices. The integrals for eq. (2) and eq. (3) are most conveniently performed over helical coordinates (r, ϕ, ζ), as explained in Waldron[14] or appendix B, where they can then be translated back into the global coordinate system of choice*.

---

*It is the author's experience that Cartesian coordinates remain the most convenient choice of global coordinate system for the overall model, as translations and rotations are simple to im-

See appendix B for an explicit example of calculating the H field of a drive coil (as per eq. (2)), and appendix C for calculating the magnetic flux in a pickup or compensator coil.

3.3 Modelling the lock-in amplifier

Having calculated either the time-varying magnetic flux $\Phi(t)$ or its spectrum $\Phi(\omega)$ passing through the secondary coils, the voltage across the coils $V = -\partial\Phi/\partial t$ can be easily obtained. However, this does not represent the output voltage of the susceptometer, as the signal is typically passed into a lock-in amplifier.

As a first approximation, an "ideal" lock-in amplifier is a device which – provided a reference signal of frequency ω_0 – takes a time-varying voltage input $V_{\text{in}}(t)$, and outputs two constant DC voltages:

$$V_i = \text{Re}\left\{GV_{\text{in}}(\omega_0)\right\} ;$$
$$V_q = \text{Im}\left\{GV_{\text{in}}(\omega_0)\right\} ,$$

where $V_{\text{in}}(\omega) = \int V_{\text{in}}(t)e^{i\omega t}dt$ is the input spectrum, and G is the lock-in amplifier's nominal gain. The two outputs V_i and V_q are known as the *in-phase* and *quadrature* components.[15]

Under this idealization, the computational model of the susceptometer can be implemented efficiently, as only the ω_0 spectral component of the voltage and thus flux in the secondary coils, B field, and material response $M(H)$ need to be modelled. Noise calculations can also be limited to just the ω_0 component. In particular, if the material response is linear, the same liberties apply to the H field as well, hence the time/frequency dimensionality can be completely removed from the model.

However, this idealization is only achievable when the lock-in amplifier is operated with an infinite integration time. In practice, realistic lock-in amplifiers have a finite cut-off frequency range; this can be modelled as:

$$\tilde{V} = \int_{-\infty}^{\infty} G(\omega)V_{\text{in}}(\omega + \omega_0)\, d\omega \qquad (4)$$

where $\tilde{V} = V_i + iV_q$ encodes the two DC outputs, and $G(\omega)$ is the amplifier's frequency response (which has low-pass behaviour). In general $G(\omega)$ depends on the

plement. While cylindrical coordinates may seem attractive in cases where the coils are all parallel (since the coils' helicity only "weakly" breaks azimuthal symmetry, permitting expansions in cylindrical harmonics), the implementation of vibrational calculations will be difficult, and the computational cost of the integrals dwarfs any savings from choosing a more symmetrical basis.
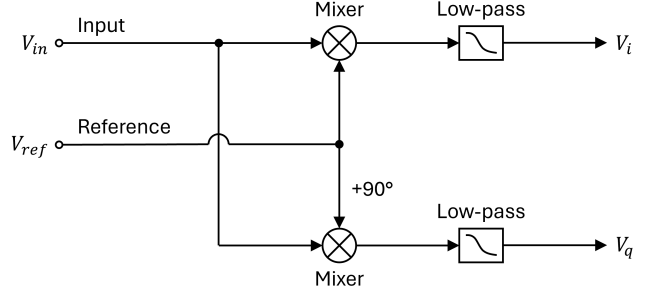

Fig. 4: Circuit schematic of a typical lock-in amplifier.

amplifier's design; e.g. a single-stage RC filter of time constant T would have $G(\omega) \propto (1 - i\omega T)^{-1}$.[16]

3.4 Frequency broadening

To further complicate matters, AC susceptibility measurements in practice tend to involve a sweep over the experimental parameters, including the frequency ω of the AC field and the magnitude H_0 of the DC field, in order to explore the behaviour of $\chi(\omega)$. As such, it would not be correct to model the driving field as an eternal static DC component plus a constant AC component (i.e. *steady-state*).

However, inputting the full time signal with time-changing parameters would be infeasible, as a wide range of parameters would require an extremely long signal to be stored and calculated. This is also unnecessarily detailed. Instead, these parameter sweeps should be interpreted as a "broadening" in the frequency spectrum of the steady-state input, but with otherwise no change to the response functions.

The simplest example would be a discrete sweep, where the experimental parameters are held constant over a time period T (with a steady input signal) and then changed discontinuously to a new set of values. Where $I(\{p_n\}, t)$ represents a steady-state input signal under some set of experimental parameters $\{p_n\}$, the full time signal can be written as:

$$I(t) = \begin{cases} \dots & \dots \\ I(\{p_{n-1}\}, t) & t_{n-1} \le t < t_n \\ I(\{p_n\}, t) & t_n \le t < t_{n+1} \\ \dots & \dots \end{cases}$$

$$= \sum_n \text{rect}\left(\frac{t - t_n}{T} - \frac{1}{2}\right) I(\{p_n\}, t)$$

where $\text{rect}(u)$ is the rectangular function. A Fourier

transform yields:

$$I(\omega) = \sum_n \int_{-\infty}^{\infty} \left[T \operatorname{sinc}\left(\frac{\omega' T}{2}\right) e^{-i\omega'(t_n + \frac{1}{2}T)} \right.$$
$$\left. I(\{p_n\}, \omega - \omega') \right] d\omega' .$$

In other words, the spectrum of the full signal with time-changing parameters is equivalent to the sum of the steady-state signals, but each convolved by the sinc window and time-translation operator. Assuming translational symmetry in time, this indicates that the system can be studied for each set of experimental parameters independently in steady-state, but with a broadening of $\delta\omega \sim 2\sqrt{3}/T$ in the input spectrum.

This frequency broadening also affects the response $G(\omega)$ of the lock-in amplifier, since it takes the driving current as the reference signal, which should therefore be also convolved with the same sinc window.

4 Material response

The application of the H field from the drive coil results in a response $M(H)$ in the sample, which ultimately gives rise to the B field. Thus an accurate model of $M(H)$ for expected samples is of key importance.

In this section, it is assumed that the sample's presence does not affect $\mathbf{H}(\mathbf{r})$ in the interior, i.e. calculations may proceed from the H field generated by the drive coil as-is without consideration for interface conditions. The treatment of such interfaces is covered in section 5.3.

4.1 Modelling anisotropy

In general there is no expectation that $\mathbf{M}(\mathbf{H})$ is parallel to $\mathbf{H}$. However, the magnetic response is expected to have the same symmetry as the underlying material itself; hence, in solid lattices, there exists three orthogonal *principal axes* where an H field applied purely along the axis will produce a magnetization $M(H)$ parallel to it.[1]*

As such, the vector field $\mathbf{M}(\mathbf{H})$ can be computed along each of the three principal axes separately. Where $\hat{\mathbf{e}}_i$ for $i \in \{1, 2, 3\}$ is the unit direction vector for the ith principal axis, this can be expressed as:

$$\mathbf{M}(\mathbf{H}) = \sum_{i=1}^{3} M_i(\mathbf{H} \cdot \hat{\mathbf{e}}_i) \, \hat{\mathbf{e}}_i$$

---

*See appendix E.

where $M_i(H)$ is the scalar response for the ith principal axis. Thus, even in an anisotropic material, the magnetization can be treated as a scalar function along each of the three principal axes independently; all further sections are based on this principle.

4.2 Nonlinear anhysteretic materials

The response of a paramagnetic material can be modelled using the Brillouin function, which emerges as the result of an ensemble of non-interacting spins taking one of the $2J + 1$ possible values $\{-J, \ldots, J\}$. For an H field applied on one of the principal axes, the response $M(H)$ is:

$$M(H) = M_s \left[\frac{2J+1}{2J} \coth\left(\frac{2J+1}{2}\beta g\mu_B\mu_0 H\right) \right.$$
$$\left. - \frac{1}{2J}\coth\left(\frac{1}{2}\beta g\mu_B\mu_0 H\right) \right]$$

where M_s is the saturation magnetization, g is the Landé g-factor, μ_B is the Bohr magneton, and $\beta = 1/k_B T$ is the inverse temperature.[8]

In the classical limit, spins may take continuous values, i.e. $J \to \infty$ and $gJ \to \text{const}$. This yields Langevin paramagnetism:

$$M(H) = M_s \left[\coth\left(\frac{H}{a}\right) - \frac{a}{H} \right] \quad (5)$$

where a is some constant representing the magnetic "hardness", which is proportional to β^{-1}. Linear response is recovered in the limit of $a \to \infty$ with $\chi = M_s/3a$.

Other effects, however, can contribute an additional magnetization; for example, the Larmor precession of electrons give rise to Langevin diamagnetism, while second order Zeeman perturbations give rise to van Vleck paramagnetism in small molecules.[17] Metals and solid lattices also further exhibit Pauli paramagnetism and Landau diamagnetism, due to the effects of the delocalized electron gas.[8,18]

To first-order, these effects are linear†, and can be combined as $M = \chi_0 H$ where χ_0 may be positive or negative (depending on which effect dominates).

As such, the following expression constitutes a highly general yet simple description, capable of capturing

---

†Landau diamagnetism is linear only in the low field limit; at higher fields it exhibits de Haas-van Alphen oscillations, which are highly nonlinear.

most physical materials:

$$M(H) = M_s \left[\coth\left(\frac{H}{a}\right) - \frac{a}{H} \right] + \chi_0 H \quad (6)$$

where all of M_s, a, χ_0 may have general dependence on temperature.

4.2.1 Temperature dependence of parameters

For Langevin paramagnetism (eq. (5)), it was derived that $a \propto k_B T$ while M_s is temperature-independent; this yields $\chi \propto T^{-1}$, which is the Curie Law. This derivation, however, assumed non-interacting spins – an assumption which may not hold in real materials.

A precise account of spin-spin interactions can give rise to ferromagnetism, which is outside the scope of this section (see section 4.3). Nonetheless, in the mean field approximation, the spin-spin interactions can be modelled as a uniform Weiss field, which yields Curie-Weiss Law:

$$\chi \propto \frac{1}{T - \Theta} \qquad \rightarrow \qquad a \propto T - \Theta$$

where Θ is the Weiss temperature. M_s remains temperature-independent.[18]

On the other hand, the temperature dependence of χ_0 depends on the dominant effect. For example, Langevin diamagnetism predicts temperature-independent χ_0, while van Vleck paramagnetism for small molecules predicts Curie-like behaviour with constant offset $\chi_0 \propto 1/T + C$, if there are no excitations comparable to $k_B T$, or complicated dependence on temperature otherwise.[17]

Pauli paramagnetism typically dominates in solid lattices, especially at low field strengths; it predicts temperature dependence:

$$\chi_0 \propto \int g(\epsilon) \frac{\partial f(\epsilon, \mu, T)}{\partial \epsilon} \, d\epsilon \quad (7)$$

where $g(\epsilon)$ is the density of states in the conduction band, and $f(\epsilon, \mu, T) = (\exp[(\epsilon - \mu)/k_B T] + 1)^{-1}$ is the Fermi-Dirac distribution.[19]

In the low field limit where linearity holds, for three-dimensional systems Landau diamagnetism simply reduces the effects of Pauli paramagnetism by a factor of 2/3; as such eq. (7) remains unaffected in applicable systems.[20]
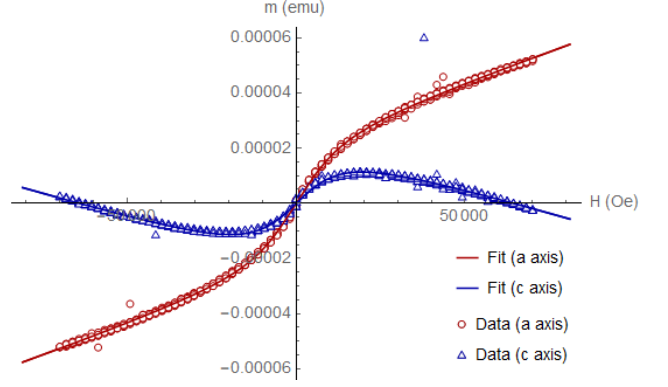

Fig. 5: DC magnetic moment of a FeSb$_2$ sample under varying DC field applied along the a and c axes, at $T = 1.8\,\text{K}$. The data shown above is an overlay of four runs wherein the sample was field-cooled at 0, 500 Oe, 1 T, and 7 T; no difference is observed between different field coolings. The best-fit curve for the a axis was generated using eq. (6) with best-fit parameters $M_s = 73.8 \pm 1.3\,\text{A/m}$, $a = (4.28 \pm 0.08) \times 10^5\,\text{A/m}$, and $\chi_0 = (1.63 \pm 0.03) \times 10^{-5}$; and for the c axis $M_s = 78 \pm 3\,\text{A/m}$, $a = (4.5 \pm 0.2) \times 10^5\,\text{A/m}$, and $\chi_0 = -(1.40 \pm 0.05) \times 10^{-5}$.
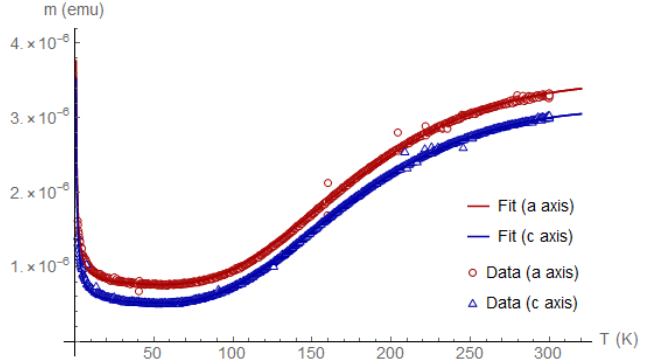

Fig. 6: DC magnetic moment of a FeSb$_2$ sample under varying temperature, while subject to a constant H field of 500 Oe along the a and c axes. The best-fit curve for the a axis was generated using eq. (8) with best-fit parameters $\chi_A = 0.02$, $E_g = 96\,\text{meV}$, $W = 3\,\text{meV}$, $\chi_B = (5.50 \pm 0.07) \times 10^{-5}$, and $\chi_C T_C = (1.50 \pm 0.03) \times 10^{-4}\,\text{K}$; and for the c axis $\chi_A = 0.01$, $E_g = 94\,\text{meV}$, $W = 3\,\text{meV}$, $\chi_B = (3.62 \pm 0.05) \times 10^{-5}$, and $\chi_C T_C = (1.50 \pm 0.02) \times 10^{-4}\,\text{K}$.

4.2.2 Experimental confirmation

To satisfy the author's desire to validate the model proposed in section 4.2 experimentally, a sample of FeSb$_2$ was placed in a Quantum Design MPMS® 3, with its DC magnetic moment along the a and c axes measured under a range of applied DC fields and temperatures. See appendix F for details.

FeSb$_2$ is an anisotropic Kondo insulator which exhibits paramagnetism on the a and b axes, and diamagnetism on the c axis.[21] It was found that the magnetic responses $M(H)$ along the a and c axes are

well-described by eq. (6), as seen in fig. 5.

The magnetic response is dominated by Pauli paramagnetism, which is dependent on the density of states in the conduction band. Previous literature[22,23] indicates that the density of states of $FeSb_2$ can be well-approximated by two narrow rectangular bands of width W and gap $E_g = 2\Delta$. Evaluating eq. (7) for this density of states, and inserting the result into eq. (6) for a small constant applied H field, gives temperature-dependent magnetization:

$$\frac{M(T)}{H} \approx -\chi_A \frac{e^{\beta\Delta}(1 - e^{\beta W})}{(1 + e^{\beta\Delta})(1 + e^{\beta(\Delta+W)})} \\ + \chi_B + \chi_C \frac{T_C}{T} \quad (8)$$

where χ_A, χ_B are integration constants from eq. (7), while the third term emerges from Curie Law $a = M_s T / 3\chi_C T_C$.

It was found that the temperature dependence of the magnetization $M(T)$ along the a and c axes are well-described by eq. (8), as seen in fig. 6.

These experimental findings thus demonstrate that the model proposed in section 4.2 is valid, with response $M(H)$ at a given temperature being well-described by eq. (6), and that the effect-specific description of temperature dependence is appropriate (at least for materials dominated by Pauli paramagnetism). Furthermore, the independent responses of the a and c axes demonstrates that it is valid to decouple the vector magnetic response into three independent scalar responses on the principal axes, for an anisotropic material.

4.3   Hysteretic materials

The models proposed so far predict no frequency dependence on the (differential) susceptibility $\chi = \partial M / \partial H$, as there is no inherent timescale in the model. This can be intuited by reversibility and rescaling arguments.

Instead, frequency dependence in the AC susceptibility $\chi(\omega)$ is inherently linked to hysteresis. This is a highly complex topic, with many different approaches;[24] this section shall be limited to just ferromagnetism, as a well-established example of magnetic hysteresis.

A physically-accurate microscopic description of ferromagnetism would be unnecessarily detailed for a practical implementation. Instead, a macroscopic description, e.g. the Jiles-Atherton model, is preferred.

In the Jiles-Atherton model, a material is described

Parameter	Description
α	Mean field self-interaction strength
M_s	Same meaning as eq. (5)
a	Same meaning as eq. (5)
k	Demagnetization energy cost
c	Reversibility parameter

Table 1: Jiles-Atherton parameters.

by five parameters, as shown in table 1. When the material is subjected to a time-changing field $H(t)$, its magnetization $M(H(t), t)$ can be expressed as a combination of a reversible anhysteretic part $M_{an}(H_e)$ and an irreversible part $M_{ir}(t)$:

$$M(H,t) = \frac{c}{1+c} M_{an}(H_e) + \frac{1}{1+c} M_{ir}(t)$$

where $H_e = H + \alpha M(H,t)$ is the effective field "screened" by self-interactions. The anhysteretic part follows the same Langevin model (eq. (5)) as in section 4.2, but depends on effective field H_e rather than bare field H.

The irreversible part evolves over time as:

$$\frac{d}{dt} M_{ir} = \frac{M_{an} - M}{k \, \mathrm{sgn}\,(dH/dt) - \alpha \, (M_{an} - M)} \frac{dH}{dt}$$

where $\mathrm{sgn}(u)$ is the sign function. With this model, $M(H,t)$ should be calculated from $H(t)$ and initial conditions in discrete time steps, as the evolution of M_{an} and M_{ir} depend on past values.[25]

See Xue et al.[26] for a refinement of the model, and Wang et al.[27] for a discussion of fitting the model to real data.

5   Modelling noise (and other non-idealities)

It is only after constructing the computational model (and writing the appropriate code) that the effects of noise and other non-idealities on the AC susceptometer can be analysed. Fortunately, so long as the underlying model is general, it is easy to "insert" these effects as perturbations.

5.1   Mechanical vibrations

The single greatest source of noise in practical AC susceptometers is mechanical vibrations, e.g. from cryostat pumps; as such a model of vibration-induced noise is of interest.[6]

External noise sources generate time-fluctuating forces on the components of a susceptometer, which respond as mechanical oscillators according to their normal modes of vibration. The external forces are stochastic in nature, so a time-domain description $\mathbf{F}(t)$ is unsuitable, but the *acoustic power spectrum* $P(\omega)$ is often known.

Let us consider only bulk vibrations of the susceptometer's components, i.e. where each coil/sample moves as a rigid body. Each component can be modelled on each of its axes as a damped harmonic oscillator of natural frequency ω_0 and damping ratio γ, such that the response function to an external force per mass $f(t)$ on the same axis is:

$$ x(\omega) \;=\; \frac{1}{\omega_0{}^2 - \omega^2 - i\gamma\omega} \; f(\omega) \,. $$

Note that any given component may have different values of ω_0 and γ for each of its axes. In this case $f(\omega)$ and thus also $x(\omega)$ are stochastic functions, but the expected variance can be computed as:

$$ \langle x(\omega)x(\omega')\rangle \;\propto\; \frac{P(\omega)}{(\omega_0{}^2 - \omega^2)^2 + \gamma^2\omega^2} \; 2\pi\delta(\omega - \omega') $$

for each axis. Following from this, the velocity spectrum is $\langle v(\omega)v(\omega')\rangle = \omega^2 \langle x(\omega)x(\omega')\rangle$.

Assuming that the external driving force is uncorrelated between different axes, we may define:

$$ \langle A_i^2(\omega)\rangle \;:=\; \frac{k_i P(\omega)}{(\omega_{0,i}{}^2 - \omega^2)^2 + \gamma_i^2\omega^2} \;; $$

$$ \langle x_i(\omega)x_j(\omega')\rangle \;=\; \langle A_i^2(\omega)\rangle \, 2\pi\delta(\omega - \omega') \, \delta_{ij} $$

(9)

for axes $i, j \in \{1, 2, 3\}$, where k_i is the "inverse mass" of the axis.

5.1.1 Vibrations of the secondary coils

In the magnetostatic limit, we can neglect relativistic effects* and adopt Galilean relativity.

Given the $\mathbf{B}(\mathbf{r}, t)$ field, in the frame of the sample/reference coil vibrating with velocity $\mathbf{v}(t)$ the time derivative is simply replaced by:

$$ \frac{d\mathbf{B}}{dt} \;\;\mapsto\;\; (\mathbf{v}(t) \cdot \nabla)\,\mathbf{B} \,+\, \frac{d\mathbf{B}}{dt} $$

---

*Unless vibrations are comparable to the speed of light.

hence eq. (3) should be modified to be:

$$ V_{\partial\Sigma}(t) \;=\; -\iint_\Sigma (\mathbf{v} \cdot \nabla)\,\mathbf{B} \cdot d\mathbf{S} - \frac{d}{dt}\iint_\Sigma \mathbf{B} \cdot d\mathbf{S} \,. $$

The first term is identified as the vibration-induced voltage noise $\delta V(t)$, which enters the final measurement. A Fourier transform gives:

$$ \delta V(\omega) \;=\; -\int d\omega' \iint_\Sigma (\mathbf{v}(\omega') \cdot \nabla)\,\mathbf{B}(\omega - \omega') \cdot d\mathbf{S} $$

hence the mean square is:

$$ \langle \delta V^2(\omega)\rangle \;=\; -\int d\omega' \sum_{i=1}^{3} \Bigg[\omega'^2 \langle A_i^2(\omega')\rangle \\ \left(\iint_\Sigma \nabla_i\,\mathbf{B}(\omega - \omega') \cdot d\mathbf{S} \right)^2 \Bigg] $$

where $\langle A_i^2(\omega')\rangle$ is given by eq. (9). This vibration-induced noise results in frequency mixing based on the distribution of $\langle A_i^2(\omega')\rangle$, so that the frequency-specific voltage filtered by the lock-in amplifier is affected by the *entire* spectrum of $\mathbf{B}(\omega)$.

If the vibrations of the sample and reference coils are considered to be independent, then the total noise is simply the sum of variances $\langle \delta V^2 \rangle = \langle \delta V^2_{\mathrm{smpl}}\rangle + \langle \delta V^2_{\mathrm{ref}}\rangle$, i.e. the magnitudes are summed in quadrature. Otherwise, the expression above must be modified to account for correlations; in particular, if the coils are mechanically linked, then the noise will be much smaller than the independent estimate, as the opposing directions of the coils result in the induced voltages mostly "cancelling" out.

5.1.2 Vibrations of the sample and drive coil

Applying the same reasoning as before, the $\mathbf{H}(\mathbf{r}, t)$ field generated by a drive coil vibrating with displacement $\mathbf{x}_{\mathrm{dr}}(t)$ gives:

$$ \mathbf{H}(\mathbf{r}, t) \;\;\mapsto\;\; (\mathbf{x}_{\mathrm{dr}}(t) \cdot \nabla)\,\mathbf{H} \,+\, \mathbf{H}(\mathbf{r}, t) $$

while a sample vibrating with displacement $\mathbf{x}_{\mathrm{sm}}(t)$ experiences:

$$ \mathbf{H}(\mathbf{r}, t) \;\;\mapsto\;\; -(\mathbf{x}_{\mathrm{sm}}(t) \cdot \nabla)\,\mathbf{H} \,+\, \mathbf{H}(\mathbf{r}, t) \,. $$

Assuming a susceptometer with balanced secondary coils, the induced change in the H field does not induce

a voltage change in the secondary coils directly. However, there is an induced change in the sample magnetization $\delta\mathbf{M} \approx \chi\delta\mathbf{H}$, which will be detected as a *relative* noise in the magnitude of χ itself. The relative voltage noise is thus:

$$\frac{\sqrt{\langle\delta V^2\rangle}}{V} = \frac{\sqrt{\langle\delta H^2\rangle}}{H}$$

where the absolute H field noise has variance:

$$\langle\delta H^2(\omega)\rangle = \int d\omega' \sum_{i=1}^{3} \left[\langle A_i^2(\omega')\rangle \left(\nabla_i H(\omega - \omega')\right)^2 \right]$$

independently for each of the drive coil's or sample's vibration.

5.2   External electromagnetic radiation

For a well-designed susceptometer with balanced secondary coils, an external time-varying H or E field will not induce any net voltage if it is spatially uniform; as such, only *incoherent* external radiation with coherence length or width smaller than the susceptometer's lengthscale can induce any noise.

It should be noted that the "mains noise" often suffered in experiments – where measurements at frequencies harmonic to the mains electrical grid are very noisy – may not be caused by direct electromagnetic induction, but rather by the acoustic power spectrum of cryostat pumps etc. containing strong components at the mains frequency's harmonics.

Nonetheless, incoherent external radiation can induce noise in the measurement.

Consider external radiation with spectral intensity $I(\omega)$ and coherence length $\xi(\omega)$. At a given frequency ω, the B field strength of the radiation has correlation:

$$\langle B_i(\mathbf{r}, \omega) B_j(\mathbf{r}', \omega')\rangle = \frac{2}{3}\sqrt{\mu_0{}^3\epsilon_0}\, I(\omega)$$
$$2\pi\delta(\omega - \omega')\delta_{ij} \exp\left(-\frac{|\mathbf{r} - \mathbf{r}'|}{\xi(\omega)}\right).$$

Let Σ be the *combined* surfaces bounded by the secondary coils, accounting for winding directions; in a balanced susceptometer $\iint_\Sigma d\mathbf{S} = \mathbf{0}$. The noise is then:

$$\delta V(\omega) = -\iint_\Sigma \frac{\partial\mathbf{B}(\mathbf{r}, \omega)}{\partial t} \cdot d\mathbf{S}(\mathbf{r})$$

which has variance:

$$\langle\delta V^2(\omega)\rangle = -\frac{2}{3}\omega^2\sqrt{\mu_0{}^3\epsilon_0}\, I(\omega)$$
$$\iint_\Sigma \iint_\Sigma \exp\left(-\frac{|\mathbf{r} - \mathbf{r}'|}{\xi(\omega)}\right) d\mathbf{S}(\mathbf{r}) \cdot d\mathbf{S}(\mathbf{r}').$$

5.3   Eddy currents and interface conditions

The magnetostatic equations (eq. (1)) result in continuity conditions for the surface-normal B field and the surface-parallel H field at interfaces between materials; these conditions are enforced by the induction of eddy currents on the surface.[12]

Eddy currents on the sample's surface thus result in the H field inside the sample differing to the H field generated by the drive coil. This is particularly notable in conductive samples.

Furthermore, eddy currents generated in the finite-thickness wires of the secondary coils, in the metallic walls of the cryostat, etc. will also "reflect" the H field generated by the drive coil; as such the steady-state H field generated by the drive coil may not correspond to a direct evaluation of the Biot-Savart Law on the drive coil's current density distribution.

The overall effect is that the actual H field inside the sample may be both screened in magnitude and phase-shifted, possibly non-uniformly, compared to the calculated H field.

Analysis of this effect is outside the scope of this work; see Goldfarb and Minervini[9], Pippard[28], and Zijlstra[29] for brief discussions of the phenomenon.

5.4   Thermal dissipation

Due to Joule heating in the drive coil, as well as eddy currents induced on the surface, the sample's temperature is often raised above the nominal temperature of the cryostat. This would result in a systematic error, if the experimenter naïvely takes the cryostat temperature as the "true" temperature.

In principle, this heating can be modelled numerically; but in practice this is accounted for by attaching a thermometer to the sample (or the coils) directly, ensuring that the measured temperature is accurate.* As such this is not a significant source of error.

There is also another effect to consider, where a drive

---

*At least, this is the normal procedure for the Quantum Matter group, Cavendish Laboratory, University of Cambridge.

coil driven at frequency ω_0 produces heating power periodic at $2\omega_0$; this introduces thermally-induced oscillations at harmonics of $2\omega_0$. However:

- The lock-in amplifier only picks up signals within a narrow band of ω_0; thermally-induced oscillations may affect the measurement only if there is significant frequency down-mixing (either in the sample's magnetization, or the coils' acoustic response);

- Thermal oscillations at frequency ω decay over a characteristic length $\sqrt{2D/\omega}$ where D is the thermal diffusivity; for typical materials this is much smaller than the sample size.

as such the effect is negligible.

5.5 Impedance mismatch

Ideally, the lock-in amplifier measuring the AC voltage of the secondary coils should have infinite input impedance, as a voltmeter. Of course, a realistic amplifier would have finite input impedance, albeit still much greater than the secondary coils' impedance.

For a simple circuit like shown in fig. 3, the impedance Z_{amp} of the amplifier results in the measured voltage V_m being lower than the voltage V_{coil} induced across the secondary coils of impedance Z_{coil}:

$$V_m(\omega) \;=\; V_{\mathrm{coil}}(\omega)\frac{Z_{\mathrm{amp}}(\omega)}{Z_{\mathrm{coil}}(\omega) + Z_{\mathrm{amp}}(\omega)}$$

as well as a leakage current I_{leak}:

$$I_{\mathrm{leak}}(\omega) \;=\; V_{\mathrm{coil}}(\omega)\frac{1}{Z_{\mathrm{coil}}(\omega) + Z_{\mathrm{amp}}(\omega)}\;.$$

This leakage current results in the secondary coils generating their own H field, especially if the coils are unbalanced, at the same frequency as the measurement frequency. This would not be an issue if the impedance ratio $Z_{\mathrm{coil}}/Z_{\mathrm{amp}}$ is frequency-independent, as the leakage field and reduced voltage would simply apply a proportionality constant (which would be accounted for by calibration); but if there is a frequency dependence then this impedance mismatch may result in a spurious frequency dependence in the measured $\chi(\omega)$.

It should be noted that realistic susceptometers may involve more complicated circuitry than considered here, e.g. transformers along the signal path. Circuit analysis holds as usual, but the minimum-noise condition may not be just $Z_{\mathrm{amp}} \gg Z_{\mathrm{coil}}$.

Calculating the effects of this impedance mismatch is simple, once the computational model for the suscep-

tometer has been created. The secondary coils can simply be treated as primary coils carrying current I_{leak}, with the same code re-used to calculate the resultant H field.

6   Conclusion

As discussed across previous sections, various computational models can be constructed for each "piece" of the susceptometer to build an accurate simulation of the setup. It is clear, however, that a prediction of the susceptometer's output voltage at a specific reference frequency ω, even when the drive coil is driven only at that frequency, still requires full information about all fields' temporal behaviours, especially for noise calculations.

It is seen that neither the time-domain nor frequency-domain representation are particularly convenient – rather, a program should switch between both representations readily. For example, it is easiest to simulate the magnetization of a hysteretic material in the time domain, yet the induced voltage as a result of the B field is best calculated in the frequency domain. This can be achieved efficiently using Fast Fourier Transform (FFT) techniques.[30]

See fig. 7 for an example of how a computer program can be constructed from the principles discussed in this work. Various noise sources can then be implemented based on the discussions in section 5.

7   Further work

The author has been attempting to write an open-source software package based on the program logic shown in fig. 7, with the goal of producing a user-friendly program; in fact, this work was based on the technical difficulties encountered in doing so. Unfortunately, this program has not been completed.

The curse of dimensionality is inescapable – in order to predict noise occurring at a signal-to-noise ratio of s, the computational model must retain a fractional resolution of at most $1/s$ on every spatial dimension, as well as on the time/frequency domain. This gives a computational complexity of at least $O(s^4)$ on both time and memory, which is resource-demanding.

Nonetheless a bespoke program for modelling the AC susceptometer, as opposed to a general-purpose EM simulation software (with multiphysics support, e.g. COMSOL), will still benefit from improved convergence rates and greater ease of examining first-order deviations. As such, it is the author's intent to continue work on the program.
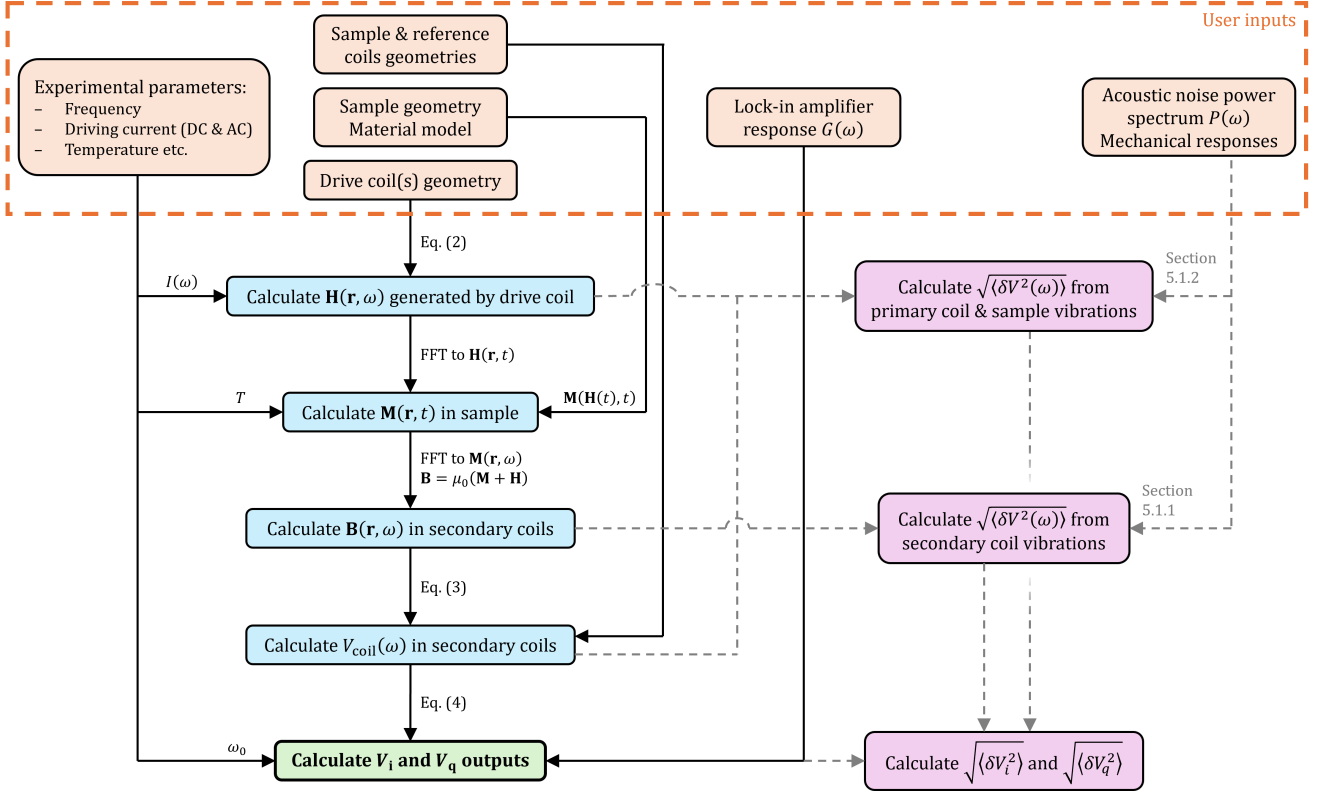
Fig. 7: Flowchart for a possible computer program, using the principles discussed in this work to simulate a susceptometer. The left side (drawn in solid arrows) is the "base" component of the program, which simulates the ideal susceptometer; note that the frequency broadening discussed in section 3.4 should already be included in the input parameters $I(\omega)$ and $G(\omega)$. The right side (drawn in dashed arrows) is an example specifically showing how vibration-induced noise can be calculated from the base results. Other noise sources can be implemented in a similar manner.

References

[1] T.G. Mackay and A. Lakhtakia. *Electromagnetic Anisotropy and Bianisotropy*. World Scientific, 2nd edition, 2009. doi: 10.1142/7515.

[2] S.C. Lim, J. Osman, and D.R. Tilley. Calculation of nonlinear magnetic susceptibility tensors for a ferromagnet. *J. Phys. D: Appl. Phys.*, 32(7):755, 1999. doi: 10.1088/0022-3727/32/7/002.

[3] D. Martien. Introduction to: AC susceptibility. Technical report, Quantum Design, 2001.

[4] S. Mugiraneza and A.M. Hallas. Tutorial: A beginner's guide to interpreting magnetic susceptibility data with the Curie-Weiss law. *Commun. Phys.*, 5(95), 2022. doi: 10.1038/s42005-022-00853-y.

[5] R.W. Stark and L.R. Windmiller. Theory and technology for measuring the de Haas-van Alphen type spectra in metal. *Cryogenics*, 8(5):272–281, 1968. doi: 10.1016/S0011-2275(68)80002-5.

[6] J.R. Anderson and D.R. Stone. Experimental methods for the de Haas-van Alphen effect. In R.V. Coleman, editor, *Solid State Physics*, volume 11 of *Methods in Experimental Physics*, pages 33–65. Academic Press, 1974. doi: 10.1016/S0076-695X(08)60175-1.

[7] N.R. Dilley and M. McElfresh. *AC Susceptometry*, pages 63–90. Springer International Publishing, 2021. doi: 10.1007/978-3-030-70443-8.

[8] C. Kittel. *Introduction to Solid State Physics*. Wiley, 8th edition, 2004.

[9] R.B. Goldfarb and J.V. Minervini. Calibration of AC susceptometer for cylindrical specimens. *Rev. Sci. Instrum.*, 55(5):761–764, 1984. doi: 10.1063/1.1137813.

[10] J.R. Pierce. Physical sources of noise. *Proc. IRE*, 44(5):601–608, 1956. doi: 10.1109/JRPROC.1956.275123.

[11] M. Nikolo. Superconductivity: A guide to alternating current susceptibility measurements and alternating current susceptometer design. *Am. J. Phys.*, 63(1):57–65, 1995. doi: 10.1119/1.7770.

[12] D.J. Griffiths. *Introduction to Electrodynamics*. Cambridge University Press, 4th edition, 2017. doi: 10.1017/9781108333511.

[13] M. Sands R. Feynman, R.B. Leighton. *Magneto-statics*, volume 2, chapter 13. Pearson/Addison-Wesley, 2006.

[14] R.A. Waldron. A helical coordinate systems and its applications in electromagnetic theory. *Q. J. Mech. Appl. Math.*, 11(4):438–461, 1958. doi: 10.1093/qjmam/11.4.438.

[15] C.A. Stutt. Low-frequency spectrum of lock-in amplifiers. Technical report, Massachusetts Institute of Technology, Research Laboratory of Electronics, 1949.

[16] D.A. van Baak and G. Herold. Response of a lock-in amplifier to noise. *Am. J. Phys.*, 82(8):785–797, 2014. doi: 10.1119/1.4873915.

[17] J.H. van Vleck. On dielectric constants and magnetic susceptibilities in the new quantum mechanics: part III – application to dia- and paramagnetism. *Phys. Rev.*, 31(4):587–613, 1928. doi: 10.1103/PhysRev.31.587.

[18] N. Ashcroft and N.D. Mermin. *Solid State Physics*. Saunders College Publishing, 1976.

[19] W. Pauli. Zur Quantenmechanik des magnetischen Elektrons. *Z. Phys.*, 43:601–623, 1927. doi: 10.1007/BF01397326.

[20] L.D. Landau. Diamagnetismus der Metalle. *Z. Phys.*, 64:629–637, 1930. doi: 10.1007/BF01397213.

[21] A. Eaton. *$FeSb_2$: a riddle, inside an insulator, wrapped in a metal; Electric and magnetic properties of the unconventional insulator iron diantimonide*. PhD thesis, University of Cambridge, 2022.

[22] V. Jaccarino, G.K. Wertheim, J.H. Wernick, L.R. Walker, S.L. Bud'ko, and S. Arajs. Paramagnetic excited state of FeSi. *Phys. Rev.*, 160(3):476–482, 1967. doi: 10.1103/PhysRev.160.476.

[23] C. Petrovic, Y. Lee, T. Vogt, N.Dj. Lazarov, S.L. Bud'ko, and P.C. Canfield. Kondo insulator description of spin state transition in $FeSb_2$. *Phys. Rev. B*, 72(4):045103, 2005. doi: 10.1103/PhysRevB.72.045103.

[24] E.D. Torre. *Magnetic Hysteresis*. Wiley-IEEE Press, 1999.

[25] D.C. Jiles and D.L. Atherton. Theory of ferromagnetic hysteresis. *J. Magn. Magn. Mater.*, 61(1):48–60, 1986. doi: 10.1016/0304-8853(86)90066-1.

[26] G. Xue, H. Bai, T. Li, Z. Ren, X. Liu, and C. Lu. Numerical solving method for Jiles-Atherton model and influence analysis of the initial magnetic field on hysteresis. *Mathematics*, 10 (23):4431, 2022. doi: 10.3390/math10234431.

[27] X. Wang, D.W.P. Thomas, M. Sumner, J. Paul, and S.H.L. Cabral. Numerical determination of Jiles-Atherton model parameters. *COMPEL*, 28 (2):493–503, 2009. doi: 10.1108/03321640910929344.

[28] A.B. Pippard. Commentary on a conjecture of Shoenberg's concerning the de Haas-van Alphen effect. *Proc. R. Soc. Lond.*, 272(1349):192–206, 1963. doi: 10.1098/rspa.1963.0049.

[29] H. Zijlstra. *Experimental Methods in Magnetism*. North-Holland Publishing, 1967.

[30] M. Frigo and S.G. Johnson. The design and implementation of FFTW3. *Proc. IEEE*, 93(2):216, 2005. doi: 10.1109/JPROC.2004.840301.

[31] A. Sommerfeld. Über den Wechselstromwiderstand der Spulen. *Ann. Phys.*, 329(14):609–634, 1907. doi: 10.1002/andp.19073291402.

[32] M. Sands R. Feynman, R.B. Leighton. *Tensors*, volume 2, chapter 31. Pearson/Addison-Wesley, 2006.

[33] NonlinearModelFit, Wolfram Language & System Documentation Center, 2008. URL `https://reference.wolfram.com/language/ref/NonlinearModelFit.html`.

APPENDIX

A Principle of operation of an ideal AC susceptometer

Refer to section 2 for the description of an AC susceptometer.

A magnetic material will produce a magnetization $M(H)$ along one of its principal axes when subjected to an applied H field along the same axis. For linear materials, this is given by $M = \chi H$, but in general the behaviour of $M(H)$ is non-trivial. In particular hysteresis may occur, in which $M(H)$ is not a single-valued function of H and may depend on the past history of magnetization.

Nonetheless, the drive coil may be used to generate a spatially uniform H field, consisting of a weak AC component with a strong DC background, i.e. $H(t) = H_0 + H_1 e^{-i\omega t}$ with $|H_1| \ll |H_0|$. For a sample subjected to such a field, a Taylor expansion for the small neighbourhood around H_0 yields:

$$M(H(t)) \approx M(H_0) + \chi(\omega)H_1 e^{-i\omega t}$$

where $\chi(\omega)$ is the complex differential AC magnetic susceptibility. Noting $M(H_0)$ to be the DC magnetization, we thus see that there is also an AC magnetization with the same frequency ω and magnitude proportional to $\chi(\omega)$.

Now consider a cylindrical sample, with the sample coil wrapping tightly around it. Assuming that the sample coil is shorter than the sample, so that the internal volume of the sample coil is entirely occupied by the material, the resultant $B = \mu_0 (M + H)$ field is uniform everywhere in the sample coil, and given by:

$$B(t) \approx B_0 + \mu_0 (1 + \chi(\omega)) H_1 e^{-i\omega t}$$

for DC component B_0. Letting N_s and A_s be the number of turns and loop area of the sample coil respectively, the voltage developed across the sample coil oscillates as:

$$V_s(t) = -\frac{d\Phi}{dt} = i\omega\mu_0 N_s A_s (1 + \chi(\omega)) H_1 e^{-i\omega t}.$$

Let N_r and A_r be the number of turns and loop area of the reference coil respectively; by design $N_s A_s = N_r A_r$. In the coaxial configuration the reference coil does not contain the sample at all, hence its magnetic flux is purely the vacuum contribution. Noting that the reference coil is wound in the opposite direction of the sample coil, the total voltage in series (measured voltage) of the two coils is therefore:

$$V(t) = i\omega\mu_0 N_s A_s \chi(\omega)H_1 e^{-i\omega t}.$$

In the concentric configuration the reference coil does contain the sample. However, noting that $A_r > A_s$ and thus $N_r < N_s$, the magnetic flux contributed by the sample magnetization on the reference coil is proportional to $N_r A_s$ and thus does not fully "cancel" the signal from the sample coil. The total voltage in series of the two coils is therefore:

$$V(t) = i\omega\mu_0 (N_s - N_r) A_s \chi(\omega)H_1 e^{-i\omega t}.$$

In either case, since the H field is proportional to the current I_d in the drive coil, we have the proportionality relationship:

$$V \propto i\omega\chi(\omega)I_{d,1}$$

where the proportionality constant depends only on the coils' geometries and physical constants. Labelling this proportionality constant as L (suggesting an interpretation of "inductive coupling factor"), the AC magnetic susceptibility can be recovered easily as:

$$\chi(\omega) = -i\frac{V}{\omega L I_{d,1}}.$$

The factor of $-i$ is merely a phase factor, which can be accounted for in the lock-in amplifier. A phase-sensitive voltage measurement thus allows the real and imaginary parts of $\chi(\omega)$ to be determined separately, which gives useful information about the material properties.

It should be noted that – for realistic setups – samples are rarely cylindrical, and often much smaller than the sample coil. However (neglecting effects from eddy currents) the sample size only affects the value of L, which is accounted for in the calibration; as such the analysis holds.

All other deviations from the ideal are discussed in the main body of this work.

B Helical coordinate system

This work is based on Waldron[14].

The helical coordinates (r, ϕ, ζ) form a non-orthogonal coordinate system, well-suited for describing systems with helical symmetry. It includes a parameter p, which describes the system's pitch (i.e. the displacement along the axis of symmetry upon a rotation of 2π). For example, a coil of length l and turn number N has pitch $p = l/N$.

The helical coordinates extend over ranges $r \in [0, \infty)$, $\phi \in (-\infty, \infty)$, and $\zeta \in [-p/2, p/2)$. For a right-handed helix aligned to the z-axis, the transformation to Cartesian coordinates (x, y, z) is given by:

$$\begin{cases} x &= r \cos \phi \\ y &= r \sin \phi \\ z &= \zeta + \dfrac{p\phi}{2\pi} \end{cases}$$

Let us define, for mathematical convenience:

$$\alpha = \frac{p}{2\pi r} \quad ; \quad \beta = \sqrt{1 + \alpha^2}$$

The unit vectors, in terms of the Cartesian unit vectors, are:

$$\begin{pmatrix} \hat{\mathbf{e}}_r \\ \hat{\mathbf{e}}_\phi \\ \hat{\mathbf{e}}_\zeta \end{pmatrix} = \begin{pmatrix} \cos \phi & \sin \phi & 0 \\ -\frac{1}{\beta} \sin \phi & \frac{1}{\beta} \cos \phi & \alpha/\beta \\ 0 & 0 & 1 \end{pmatrix} \begin{pmatrix} \hat{\mathbf{e}}_x \\ \hat{\mathbf{e}}_y \\ \hat{\mathbf{e}}_z \end{pmatrix}$$

The line elements are:

$$\begin{cases} dl_r &= dr \\ dl_\phi &= \beta r \, d\phi \\ dl_\zeta &= d\zeta \end{cases}$$

The surface elements are:

$$\begin{cases} dS_r &= r \, d\phi d\zeta \\ dS_\phi &= dr d\zeta \\ dS_\zeta &= \beta r \, d\phi dr \end{cases}$$

The volume element is:

$$dV = r \, dr d\phi d\zeta$$

The metric is:

$$g = \begin{pmatrix} 1 & 0 & 0 \\ 0 & \beta^2 r^2 & \alpha r \\ 0 & \alpha r & 1 \end{pmatrix}$$

The gradient of a scalar field ψ is given by:

$$\nabla \psi = \frac{\partial \psi}{\partial r} \hat{\mathbf{e}}_r + \beta \left(\frac{1}{r} \frac{\partial \psi}{\partial \phi} - \alpha \frac{\partial \psi}{\partial \zeta} \right) \hat{\mathbf{e}}_\phi$$
$$+ \left(\beta^2 \frac{\partial \psi}{\partial \zeta} - \frac{\alpha}{r} \frac{\partial \psi}{\partial \phi} \right) \hat{\mathbf{e}}_\zeta$$

The Laplacian of ψ is given by:

$$\nabla^2 \psi = \frac{1}{r} \frac{\partial}{\partial r} \left(r \frac{\partial \psi}{\partial r} \right) + \frac{1}{r^2} \frac{\partial^2 \psi}{\partial \phi^2}$$
$$+ \beta^2 \frac{\partial^2 \psi}{\partial \zeta^2} - \frac{2\alpha}{r} \frac{\partial^2 \psi}{\partial \phi \partial \zeta}$$

For a vector $\mathbf{V}$ with Cartesian components (V_x, V_y, V_z), its corresponding helical components are:

$$\begin{pmatrix} V_r \\ V_\phi \\ V_\zeta \end{pmatrix} = \begin{pmatrix} \cos \phi & \sin \phi & 0 \\ -\beta \sin \phi & \beta \cos \phi & 0 \\ \alpha \sin \phi & -\alpha \cos \phi & 1 \end{pmatrix} \begin{pmatrix} V_x \\ V_y \\ V_z \end{pmatrix}$$

and the inverse transformation is:

$$\begin{pmatrix} V_x \\ V_y \\ V_z \end{pmatrix} = \begin{pmatrix} \cos \phi & -\frac{1}{\beta} \sin \phi & 0 \\ \sin \phi & \frac{1}{\beta} \cos \phi & 0 \\ 0 & \alpha/\beta & 1 \end{pmatrix} \begin{pmatrix} V_r \\ V_\phi \\ V_\zeta \end{pmatrix}$$

The divergence of a vector field $\mathbf{V}$ is given by:

$$\nabla \cdot \mathbf{V} = \frac{1}{r} \frac{\partial}{\partial r} (r V_r) + \frac{1}{\beta r} \frac{\partial V_\phi}{\partial \phi} + \frac{\partial V_\zeta}{\partial \zeta}$$

and the curl of $\mathbf{V}$ is:

$$\nabla \times \mathbf{V} = \left[\left(\frac{1}{r} \frac{\partial V_\zeta}{\partial \phi} - \alpha \frac{\partial V_\zeta}{\partial \zeta} \right) + \left(\frac{\alpha}{\beta r} \frac{\partial V_\phi}{\partial \phi} - \beta \frac{\partial V_\phi}{\partial \zeta} \right) \right] \hat{\mathbf{e}}_r$$
$$+ \beta \left[\frac{\partial V_r}{\partial \zeta} - \frac{\partial V_\zeta}{\partial r} - \frac{\partial}{\partial r} \left(\frac{\alpha V_\phi}{\beta} \right) \right] \hat{\mathbf{e}}_\phi$$
$$+ \left[\left(\frac{1}{\beta r} \frac{\partial}{\partial r} (r V_\phi) + \frac{\alpha^2}{\beta} \frac{\partial V_\phi}{\partial r} \right) - \left(\frac{1}{r} \frac{\partial V_r}{\partial \phi} - \alpha \frac{\partial V_\zeta}{\partial r} \right) \right] \hat{\mathbf{e}}_\zeta$$

The vector Laplacian has been omitted from this text, as its expression is too unwieldy for sensible typesetting.

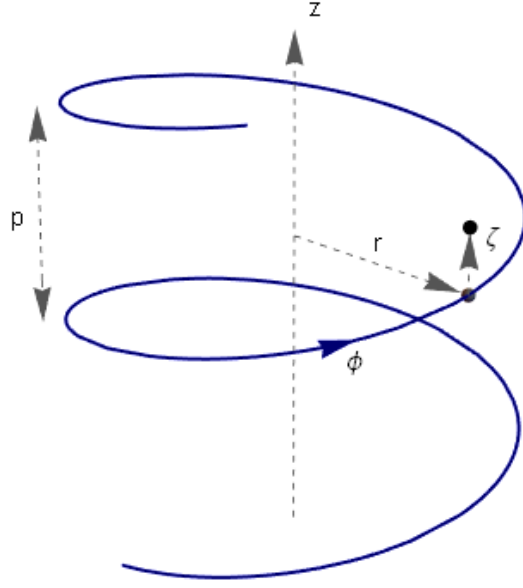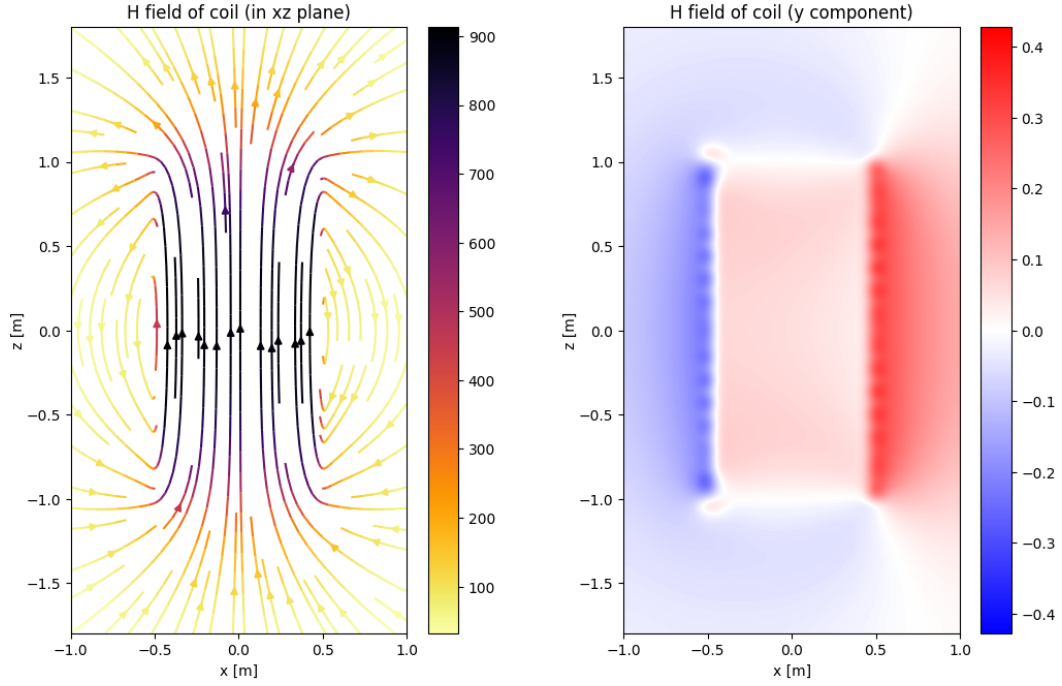Fig. 8: Helical coordinates, as discussed in appendix B.

Fig. 9: Example **H** field generated by a coil with parameters $N = 2000$, $R = 0.5\,\mathrm{m}$, and $l = 2\,\mathrm{m}$, wound from copper wire with thickness $a = b = 1\,\mathrm{mm}$ and carrying an AC current of $I = 1\,\mathrm{A}$ at $60\,\mathrm{Hz}$; this plot was calculated using the expressions laid out in appendix C. Note that the right-handed coil generates a right-handed "twist" in the field, with azimuthal component $H_\phi/|\mathbf{H}| \approx 1/2250$ being comparable to coil helicity $l/2\pi NR \approx 1/3142$ as expected.

C   Example calculation of H field produced by drive coil

This appendix is in reference to section 3.2. In this example, let us consider a drive coil with N turns of inner radius R over length l, wound from wire with a rectangular cross-section (of width a radially and b axially). Using the helical coordinates introduced in appendix B, the integral for the $\mathbf{H}$ field produced by the coil when it is carrying current I is:

$$\mathbf{H}(\mathbf{r}) = \int_R^{R+a} dr' \int_{-\pi N}^{\pi N} d\phi' \int_{-b/2}^{b/2} d\zeta'$$
$$\left[r' J(r', \phi', \zeta') \frac{\hat{\mathbf{e}}_{\phi'} \times (\mathbf{r} - \mathbf{r}')}{4\pi |\mathbf{r} - \mathbf{r}'|^3} \right]$$

where, in Cartesian coordinates:

$$\hat{\mathbf{e}}_{\phi'} = \frac{1}{\sqrt{4\pi^2 N^2 r'^2 + l^2}} \begin{pmatrix} -2\pi N r' \sin\phi' \\ 2\pi N r' \cos\phi' \\ l \end{pmatrix} \quad ;$$

$$\mathbf{r}' = \begin{pmatrix} r'\cos\phi' \\ r'\sin\phi' \\ \zeta' + \frac{l\phi'}{2\pi N} \end{pmatrix} \quad ,$$

and $J(r', \phi', \zeta')$ is the magnitude of the current density in the wire (which is assumed to be parallel to the helical direction $\hat{\mathbf{e}}_{\phi'}$). This current density should account for skin effect.

In the limit of $2\pi NR \gg L$ and $R \gg a, b$, for a close-packed coil with $b = l/N$ carrying a single-component AC current I of angular frequency ω, the skin effect (obtained by enforcing the cross-sections of the wire to be equipotential surfaces) gives current density distribution:

$$k := \left(\frac{1}{\sqrt{2}} + \frac{i}{\sqrt{2}} \right) \sqrt{\mu_0 \omega \sigma (1 + \chi)} \quad ;$$

$$J(r', \phi', \zeta') \approx \frac{I J_0(kr')}{b \int_R^{R+a} J_0(kr'') dr''} \quad ,$$

where μ_0 is the vacuum permeability, σ is the wire's conductivity, χ is the wire's magnetic susceptibility (assuming linear response), and $J_\alpha(u)$ is the Bessel function of the first kind.

Owing to the exponential growth of $J_0(kr')$, in cases where R is much larger than the skin depth $1/\mathrm{Re}(k)$ the current density is dominated by the outermost layer of the coil, which allows further approximation:

$$J(r', \phi', \zeta') \approx \frac{I}{b} \delta(r' - R - a)$$

and reduces the three-dimensional integral into two dimensions, greatly reducing computational cost.

The above expressions can be placed directly into a numerical integrator (e.g. SCIPY) for evaluation. These are valid across the range of all frequencies ω, but do require the geometrical approximations to be applicable (helicity is only accounted for "at first order"). For a general time-varying signal $I(t)$, the above calculations can be used to obtain the frequency spectrum $\mathbf{H}(\mathbf{r}, \omega)$ from $I(\omega)$, since Maxwell's Equations are linear.

For coils wound from wire with circular cross-section, see Sommerfeld[31].

D   Calculation of magnetic flux in a pickup coil

This appendix is in reference to section 3.2. In this example, we assume that the full field $\mathbf{B}(\mathbf{r})$ is already known or otherwise easily obtainable; we want to calculate the corresponding flux through a right-handed coil with N turns of inner radius R over length l centred on the origin and aligned to the z-axis.

As the cross-sections of the wire form equipotential surfaces of the electrostatic potential (with eddy currents being generated in order to enforce such conditions), only the magnetic flux passing through the surface Σ bounded by the *innermost* edge of the coil need to be considered. Using the helical coordinates introduced in appendix B, the integral for this is:

$$\Phi = \iint_\Sigma \mathbf{B}(\mathbf{r}) \cdot d\mathbf{S}$$
$$= \int_0^R \int_{-\pi N}^{\pi N} B_\zeta(r, \phi, \zeta = 0) \sqrt{r^2 + \frac{l^2}{4\pi^2 N^2}} \, d\phi \, dr$$

where, in Cartesian coordinates, the integrand is:

$$B_\zeta = \frac{l}{2\pi Nr} (B_x \sin\phi - B_y \cos\phi) + B_z$$

all evaluated at $x = r\cos\phi$, $y = r\sin\phi$, $z = l\phi/2\pi N$.

In the case that $l \ll 2\pi N R$ a cylindrical approximation can be used instead:

$$\Phi \approx \sum_{n=-N/2}^{N/2} \int_0^R \int_{-\pi}^{\pi} B_z\left(r, \theta, z = \frac{ln}{N}\right) r\, d\theta dr$$

which does not reduce computational complexity, but does simplify calculation. The relative inaccuracy introduced by this approximation is on the order of $O(h_{\text{field}} h_{\text{coil}})$, where $h_{\text{field}} \sim \max(B_\phi / |\mathbf{B}|)$ and $h_{\text{coil}} \sim l/2\pi N R$ are the helicities of the field and coil respectively.

This calculation can be performed as-is using the time-varying $\mathbf{B}(\mathbf{r}, t)$ or spectrum $\mathbf{B}(\mathbf{r}, \omega)$ of the field, yielding the flux as a function of time or frequency; the voltage measured across the coil can then be computed directly from Faraday's Law.

E Proof that the susceptibility tensor is diagonalizable for anhysteretic materials

This is an argument by R. Feynman[32].

Consider an anhysteretic material, where $\mathbf{M}(\mathbf{H})$ is a well-defined and reversible function. The differential work dW needed to change the magnetization by an infinitesimal $d\mathbf{M}$ is:

$$dW = \mathbf{H} \cdot d\mathbf{M}.$$

Now consider a closed loop in $\mathbf{H}$ space, starting and ending at some value $\mathbf{H}_0$. By reversibility, the energy cost must be zero:

$$\oint \mathbf{H} \cdot d\mathbf{M} = \oint \mathbf{H} \cdot \chi \cdot d\mathbf{H} = 0$$

where $\chi_{ij} = \partial M_i / \partial H_j$ is the differential susceptibility tensor. Let us make this loop infinitesimally small, so that χ may be considered constant. Since the integral evaluates to zero, we can simply "swap" any two directions of the loop:

$$\oint H_i \chi_{ij} dH_j = \oint H_j \chi_{ij} dH_i$$
$$= \oint H_i \chi_{ji} dH_j.$$

Since this is true for any infinitesimal loop centred on any point, $\chi_{ij} = \chi_{ji}$ must hold. Hence χ is symmetric and thus diagonalizable.

F Experimental confirmation of nonlinear material model

This appendix concerns the details of the experiment described in section 4.2.2. The sample was grown epitaxially by Nick Popiel; otherwise all other work was done by the author.

The sample of $FeSb_2$ had a mass of 2.67 ± 0.03 mg. It was mounted on an quartz glass slide using a small amount of GE varnish (see fig. 10), and lowered into the Quantum Design Magnetic Property Measurement System (MPMS®) 3 initially with the a axis facing towards the MPMS instruments.

The following sequence was then performed:

1. The sample was cooled to 1.8 K with zero applied field.

2. The DC magnetic moment of the sample was measured using a SQUID magnetometer, under a range of applied H fields sweeping from zero to $+70$ kOe to -70 kOe and back to zero in steps of 1.89 kOe. Temperature was held at 1.8 K.

3. The sample was heated back up to 300 K with zero applied field, then cooled to 1.8 K under an applied H field of 500 Oe.

4. The field sweep was repeated as per step 2.

5. The sample was heated back up to 300 K with zero applied field, then cooled to 1.8 K under an applied H field of 10 kOe.

6. The field sweep was repeated as per step 2.

7. The sample was heated back up to 300 K with zero applied field, then cooled to 1.8 K under an applied H field of 70 kOe.

8. The field sweep was repeated as per step 2.

9. The sample was heated back up to 300 K with zero applied field, then cooled to 1.8 K under an applied H field of 500 Oe.

10. While holding a constant applied H field of 500 Oe, the DC magnetic moment of the sample was measured, while being slowly heated from 1.8 K to 300 K with each measurement taken at an average of 0.37 K apart.

11. The sample was then cooled to 1.8 K under an applied H field of 70 kOe.

12. The temperature sweep was repeated as per step 10, except with applied H field held at 70 kOe.

The data for steps 2, 4, 6, and 8 is shown on fig. 11, the data for step 10 is shown on fig. 13, and the data for step 12 is shown on fig. 14.

Afterwards, the sample was removed from the MPMS, dismounted from the glass slide, and remounted onto the glass slide with the c axis facing
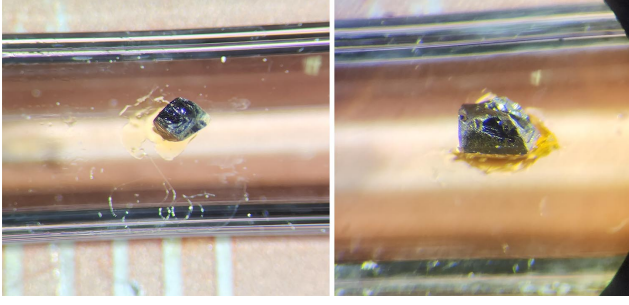
Fig. 10: Sample of FeSb$_2$ mounted on the quartz glass slide. Left: sample mounted with a axis facing the camera. Right: sample mounted with c axis facing the camera.

towards the MPMS instruments. The same sequence was then repeated for this new orientation; see fig. 12, fig. 13, and fig. 14.

The data from the field sweeps were fitted using eq. (6) according to the proposed nonlinear model; these fits were computed using MATHEMATICA's built-in NONLINEARMODELFIT function, which solves the least-squares problem via the Levenberg-Marquardt method.[33] The best-fit parameters are given in table 2 and table 3.

The data from the temperature sweeps were fitted using eq. (8) according to the Pauli-dominated model with rectangular density of states*, again using MATH-EMATICA's NONLINEARMODELFIT function. The best-fit parameters are given in tables 4 through 7.

The error estimates generated by MATHEMATICA are obtained by evaluating the second derivatives of the sum of square deviations w.r.t. the parameters at the best-fit solution; this corresponds to the standard error for a linear fit. However, this also results in very large error estimates in fitting parameters α for models involving the Boltzmann factor $e^{\beta\alpha}$ when $k_B T$ is comparable to the best-fit value of α.

In the case of the best-fit curves for the temperature sweeps, this resulted in unreasonably high uncertainties in the estimates of W, which also propagated into the uncertainties of χ_A, giving the impression that the fitted values are not statistically distinguishable from zero. This cannot be correct: a visual inspection shows that W controls the horizontal scale of the "jump" in magnetization across the $T \approx 100 - 200\,\mathrm{K}$ range, while χ_A controls the vertical scale of said jump, which is clearly non-zero in both extents.

Unfortunately, the author is presently unaware of the proper approach to resolving this anomaly.

---

*Admittedly, the 7 T temperature sweep falls outside the range of validity for the model, since the H field is not small enough to assume linearity from the Langevin part of the response; nonetheless the data fits unexpectedly well.
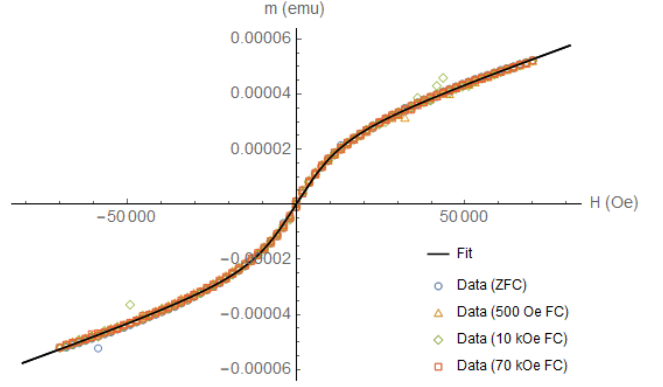

Fig. 11: DC magnetic moment under varying applied field along the a axis at $T = 1.8\,\mathrm{K}$, for different field coolings. No significant difference is observed. The best-fit curve was generated using eq. (6) with parameters given in table 2.

Parameter	Estimate	t-Statistic
$M_s V$	$(2.45 \pm 0.03) \times 10^{-8}\,\mathrm{Am^2}$	86.1
a	$(4.28 \pm 0.08) \times 10^5\,\mathrm{A/m}$	54.6
$\chi_0 V$	$(5.40 \pm 0.05) \times 10^{-15}\,\mathrm{m^3}$	104

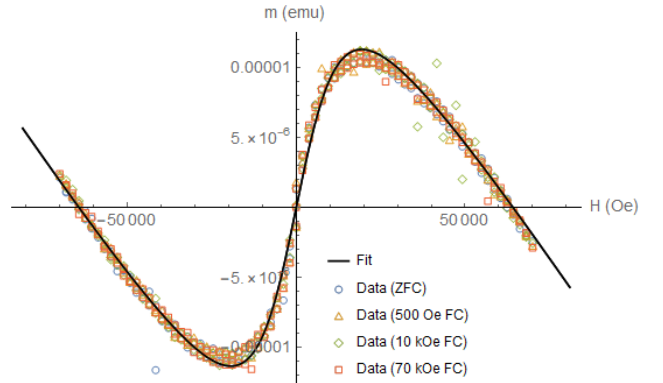Table 2: Best-fit parameters for the curve generated in fig. 11.

Fig. 12: DC magnetic moment under varying applied field along the c axis at $T = 1.8\,\mathrm{K}$, for different field coolings. No significant difference is observed. The best-fit curve was generated using eq. (6) with parameters given in table 3.

Parameter	Estimate	t-Statistic
$M_s V$	$(2.59 \pm 0.09) \times 10^{-8}\,\mathrm{Am^2}$	28.1
a	$(4.5 \pm 0.2) \times 10^5\,\mathrm{A/m}$	18.4
$\chi_0 V$	$-(4.62 \pm 0.17) \times 10^{-15}\,\mathrm{m^3}$	27.7

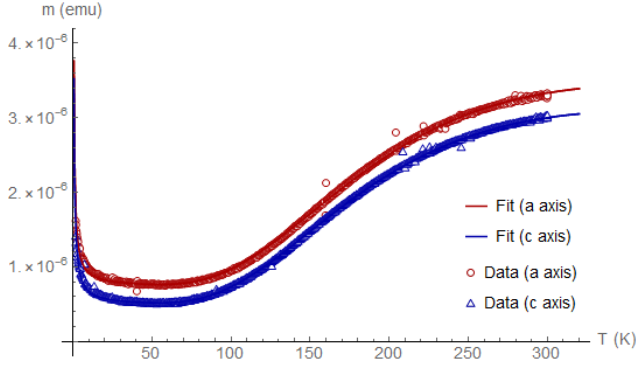Table 3: Best-fit parameters for the curve generated in fig. 12.

Fig. 13: DC magnetic moment under varying temperature, while held at $H = 500\,\mathrm{Oe}$ along the a axis. The best-fit curves were generated using eq. (8) with parameters given in table 4 and table 5.
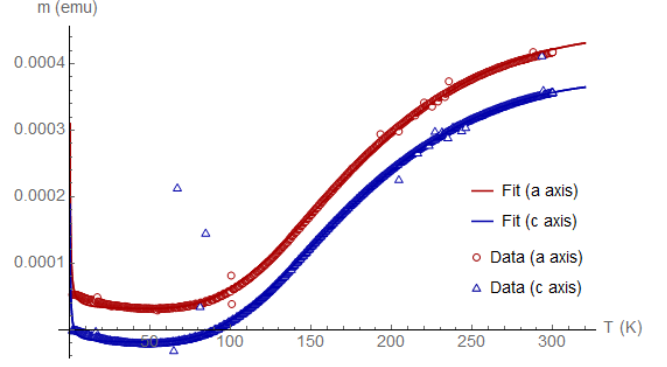

Fig. 14: DC magnetic moment under varying temperature, while held at $H = 70\,\mathrm{kOe}$ along the a axis. The best-fit curves were generated using eq. (8) with parameters given in table 6 and table 7.

Parameter	Estimate	t-Statistic
$\chi_A V$	$(0.6 \pm 2.3) \times 10^{-11}\,\mathrm{m}^3$	0.244
E_g	$96 \pm 11\,\mathrm{meV}$	8.99
W	$3 \pm 11\,\mathrm{meV}$	0.244
$\chi_B V$	$(1.823 \pm 0.006) \times 10^{-14}\,\mathrm{m}^3$	315
$\chi_C V T_C$	$(4.96 \pm 0.06) \times 10^{-14}\,\mathrm{m}^3\mathrm{K}$	84.9

Table 4: Best-fit parameters for the a axis curve generated in fig. 13.

Parameter	Estimate	t-Statistic
$\chi_A V$	$(0.1 \pm 1.4) \times 10^{-8}\,\mathrm{m}^3$	0.0949
E_g	$98 \pm 18\,\mathrm{meV}$	5.39
W	$2 \pm 19\,\mathrm{meV}$	0.0948
$\chi_B V$	$(7.43 \pm 0.09) \times 10^{-13}\,\mathrm{m}^3$	81.0
$\chi_C V T_C$	$(2.11 \pm 0.09) \times 10^{-12}\,\mathrm{m}^3\mathrm{K}$	23.0

Table 6: Best-fit parameters for the a axis curve generated in fig. 14.

Parameter	Estimate	t-Statistic
$\chi_A V$	$(0.5 \pm 1.4) \times 10^{-11}\,\mathrm{m}^3$	0.356
E_g	$94 \pm 8\,\mathrm{meV}$	12.2
W	$3 \pm 8\,\mathrm{meV}$	0.356
$\chi_B V$	$(1.201 \pm 0.005) \times 10^{-14}\,\mathrm{m}^3$	262
$\chi_C V T_C$	$(4.97 \pm 0.05) \times 10^{-14}\,\mathrm{m}^3\mathrm{K}$	109

Table 5: Best-fit parameters for the c axis curve generated in fig. 13.

Parameter	Estimate	t-Statistic
$\chi_A V$	$(0.1 \pm 2.3) \times 10^{-8}\,\mathrm{m}^3$	0.0490
E_g	$100 \pm 40\,\mathrm{meV}$	2.49
W	$0 \pm 40\,\mathrm{meV}$	0.0489
$\chi_B V$	$-(5.1 \pm 0.2) \times 10^{-13}\,\mathrm{m}^3$	23.2
$\chi_C V T_C$	$(1.6 \pm 0.2) \times 10^{-12}\,\mathrm{m}^3\mathrm{K}$	7.22

Table 7: Best-fit parameters for the c axis curve generated in fig. 14.